



Six-flux absorption-scattering models for photocatalysis under wide-spectrum irradiation sources in annular and flat reactors using catalysts with different optical properties

Ivana Grčić^{a,*}, Gianluca Li Puma^{b,*}

^a Faculty of Chemical Engineering and Technology, University of Zagreb, Marulicev trg 19, 10000 Zagreb, Croatia

^b Environmental Nanocatalysis & Photoreaction Engineering, Department of Chemical Engineering, Loughborough University, Loughborough, LE11 3TU, United Kingdom

ARTICLE INFO

Article history:

Received 2 January 2017

Received in revised form 4 April 2017

Accepted 5 April 2017

Available online 7 April 2017

Keywords:

Photocatalytic reactor

Reactor model

Optical properties

Solar irradiation

Radiation absorption

ABSTRACT

The photocatalytic oxidation of 2-hydroxybenzoic acid (2-HBA) in an annular tubular reactor (R1) and a flat rectangular open channel reactor (R2), which were irradiated with light sources emitting in the UVB, UVA and visible range of the solar radiation spectrum, and using two photocatalysts, titanium dioxide (TiO_2 P25) and Ag-modified TiO_2 P25 (Ag@TiO_2) was modeled. The local volumetric rate of photon absorption (LVRPA) in the reactors was evaluated by the six-flux absorption scattering model (SFM). The Langmuir-Hinshelwood kinetic model of the degradation of a model contaminant on irradiated aqueous suspensions of TiO_2 P25 and Ag@TiO_2 was combined with the SFM radiation model and light emission models to determine local reaction rates, and further integrated with the reactors hydrodynamics and material balances to model the degradation of 2-HBA in the photoreactors. The linear source spherical emission (LSSE) and extensive source superficial diffuse emission (ESSDE) models were compared in terms of incident and transmitted photon fluxes through the reactor. It was shown that both LSSE and ESSDE models could be successfully applied for the modeling of annular and flat reactors, considering the emission from tubular fluorescent light sources.

Since current research calls for materials with wide absorption in the solar radiation spectrum, spanning from the UV to the visible, therefore, the SFM model was adapted to consider such wide distribution. The optical properties of the photocatalysts were averaged over narrow wavelength ranges of the solar spectrum, wherein the contributions by the UVA, UVB and visible light irradiation to the LVRPA and contaminant degradation rate were separated. The effects of catalyst concentration, liquid velocity profile and the photon flux from different light sources on the 2-HBA degradation rate were explored. The "intrinsic" reaction kinetic constants of 2-HBA photocatalytic oxidation independent of reactor type, catalyst concentration, irradiance levels and hydrodynamic conditions were determined by fitting the experimental data to the model results. It was shown that the model parameters were independent of the type of catalyst used, although the catalyst exhibited significantly different optical properties.

© 2017 Elsevier B.V. All rights reserved.

1. Introduction

Heterogenous photocatalysis with semiconductor metal oxides has shown enormous potential for the conversion of environmental contaminants (organics, inorganics and bio-contaminants) [1,2]. The major benefits associated with heterogeneous photocatalysis include the potential of using solar radiation for the generation of the reactive oxidative species (ROS) and the prospective of

complete conversion of the contaminants to innocuous products. However, industrial uptake and outdoor applications of this green technology is still developing, primarily due to small quantum efficiencies and the lack of simple methods for the design, optimization and scale-up of photocatalytic reactor systems [3].

The physico-chemical phenomena that describe the interaction between reactants, catalyst and photons in photocatalytic systems are complex, since radiation emission, photon absorption, photon scattering, reactants adsorption and photochemical reactions, occur simultaneously [4–8]. Kinetics models of photocatalytic systems developed from thermal catalysis textbooks, lack the key information necessary for the design and evaluation of photocat-

* Corresponding authors.

E-mail addresses: igrcic@fkit.hr (I. Grčić), g.liipuma@lboro.ac.uk (G. Li Puma).

alytic systems, since often neglect the absorption and scattering of photons. Given the complexity of the phenomena, it is important to develop radiation and reactor models that can be applied with ease to predict the degradation of water contaminants in photocatalytic reactors having varying geometries and radiation sources. Several studies have been proposed in literature for the analysis of thin-film and tubular slurry photocatalytic reactors for water purification [9–12]. The irradiation field in these photoreactors is modeled in simple terms with either *two-flux* (TFM) or *six-flux* (SFM) absorption-scattering models [13,14] and the ability to model photoreactors with different geometries or operational modes has been shown [3]. One of the limitation of the TFM and SFM is that they use spectral-averaged catalyst optical properties to simplify the modeling procedure and this may be limiting when either wide spectrum lamp or solar radiation are used in combination with photocatalyst with absorption and scattering coefficients that vary significantly over the UV-vis radiation source spectra.

The development of highly active photocatalytic materials is another aspect of photocatalysis that has attracted intense investigations. Among the vast number of semiconductor photocatalysts, nanosized TiO₂ has shown great potential [2], however, due to the wide band gap ($E_g = 3.2$ eV) for anatase and ($E_g = 3.0$ eV) for rutile, unmodified TiO₂ absorbs only photons in the UV region (3% of the solar energy). Many studies have therefore focused on widening the absorption spectra of TiO₂ into the visible region, using dopants such as noble metals and through photosensitization of TiO₂ with organic dyes [15–20]. Among these, silver is the most common noble metal dopant for TiO₂, which narrows its band gap, exhibiting plasmonic properties which enhance the TiO₂ activity under visible light. Under solar light applications, the latter increases the cumulative degradation rates of water contaminant.

In this study, the photocatalytic oxidation of aqueous solutions of the pharmaceutical 2-hydroxy benzoic acid (2-HBA) under simulated solar irradiation was investigated using TiO₂ and Ag@TiO₂ photocatalysts. An annular reactor and a rectangular open channel (flat reactor) were used to demonstrate a simple method for the evaluation of kinetic rate constants independent from reactor geometry, hydrodynamics and radiation field. This was accomplished in simple terms by using the six-flux absorption-scattering model (SFM), which allows the calculation of the local volumetric rates of photon absorption (LVRPA), at each specific position in the photoreactors, according to the applied UVA, UVB and visible light irradiation of the simulated solar spectra. Since the development of advanced photocatalyst calls for materials with a wide absorption band, here we propose a simplified approach that takes discrete averages over narrow wavelength ranges of the solar spectrum, wherein the contributions by the UVA, UVB and visible light irradiation to the contaminant degradation rate are separated. The applied modeling approach allows the comparison of the activity of different photocatalytic materials at the net of the level of radiation absorbed in the photoreactors. The ability to predict the degradation kinetics of 2-HBA in different photoreactor geometries and under different irradiation conditions, proves the robustness of the proposed modeling approach and its applicability to the design and evaluation of photocatalytic reactors with any geometry.

2. Experimental

2.1. Catalysts and optical properties

The photocatalyst TiO₂ P25 (primary particle size 20–30 nm; specific surface area 52 m² g⁻¹; composition 78% anatase and 22% rutile) was provided by Evonik and used as received. The Ag doped TiO₂ photocatalysts (Ag@TiO₂) were prepared using the novel method including reduction of Ag⁺ to Ag⁰ nanoparticles by

chitosan as reductant [21] carried on the TiO₂ suspended in chitosan biogel (Supporting information (SI), Table S1). The synthesis yielded Ag@TiO₂ with the same microscopic characteristics, similar specific surface area and crystalline composition as the starting TiO₂ P25. The optical properties of both TiO₂ and Ag@TiO₂ were determined experimentally combining UV-vis Diffuse Reflectance Spectra (DRS) and UV-vis spectrophotometric measurements of the aqueous photocatalysts suspensions. The UV-vis spectra of the prepared samples were obtained using a DRS (Shimadzu UV-3101PC) equipped with an integrating sphere. The spectra were recorded at room temperature in the wavelength range of 200–800 nm, using BaSO₄ as a reference. The DRS reflectance results were transformed with the Kubelka–Munk function:

$$F(R) = \frac{(1 - R)^2}{2R} \quad (1)$$

where R is the reflectance of the “infinitely thick” layer of the solid [22].

The sum of the absorption κ_λ and scattering σ_λ coefficients (i.e. the extinction coefficient, β_λ) was obtained from extinction measurements (Eq. (2)) [23] of a slurry aqueous suspension:

$$\beta_\lambda = \kappa_\lambda + \sigma_\lambda = \frac{2.303 \text{EXT}_\lambda}{L} \quad (2)$$

where EXT_λ is extinction of an incident beam measured and L is cell length in cm.

The extinction spectra of catalyst suspensions (0.1–2.0 g L⁻¹) in ultrapure water prepared under darkness with magnetic stirring for 30 min, were measured using a Shimadzu UV-3101PC spectrophotometer and quartz cells (10 mm path-length, 1 mm wall thickness) after calibration of the instrument with ultrapure water. The specific extinction coefficient ($\beta_\lambda^* = \beta_\lambda / C_{\text{cat}} \text{ (m}^2 \text{ kg}^{-1}\text{)}$) calculated per unit catalyst mass concentration (C_{cat}) was obtained from the experimental values of (β_λ) applying a linear regression on the data, forcing the intercept to the axes origin. The ratio of the absorption (σ_λ) and scattering coefficients (κ_λ) was determined by DRS (Eq. (3)) from the Kubelka–Munk function (Eq. (1)).

$$F(R) = \frac{\kappa_\lambda}{\sigma_\lambda} = \frac{\kappa_\lambda^*}{\sigma_\lambda^*} \quad (3)$$

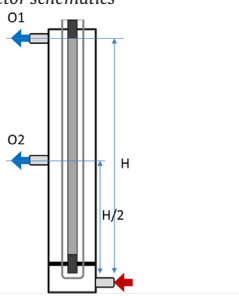
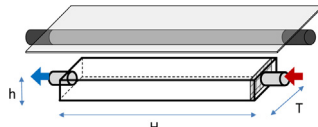
Combining Eqs. (2) and (3), both specific absorption and scattering coefficients were determined in the wavelength spectra from 200 to 800 nm.

2.2. Experimental setups

Two photoreactor configurations (Table 1) which differ significantly in their geometries were used to validate the mathematical model of photocatalytic degradation of the model contaminant (2-HBA, Pliva Pharmaceutical Company, Croatia). The outer wall of the annular photoreactor (denoted as R1) was a Pyrex glass tube (internal diameter 0.054 m, wall thickness 0.0033 m), while the inner wall was a quartz tube (external diameter 0.04 m) mounted at the axial center of the reactor. The quartz tube housed a cylindrical lamp mounted axially and centered between the flow distributing mesh and the reactor outlet. In R1, two outlets could be used (O1 and O2 ports) which allowed operation at half-length and half-volume of irradiated annular space ($V_{R1, O2} = 310 \text{ cm}^3$, $V_{R1, O1} = 620 \text{ cm}^3$). The aqueous catalyst suspension flowed continuously through its annulus between the inner and outer walls.

The flat plate photoreactor ($V_{R2} = 66 \text{ cm}^3$, denoted as R2,) with length 17 cm, width 3.9 cm and 1 cm depth had a free open surface exposed to the incident radiation. The photon flux at the surface was varied by altering the distance from the lamps (from 1.5 to 6 cm). The reactor was fitted with a zero reflectance UV protective

Table 1
Photoreactors characteristics.

R1	R2			
<i>Reactor schematics</i>				
				
<i>Dimensions</i>				
Reactor height H, cm	60 (O1) 30 (O2)			
Inner radius R_{in} , cm	2.0			
Outer radius R, cm	2.7			
Volumetric flow, Q, $\text{dm}^3 \text{ min}^{-1}$	0.2			
Used light sources	a (O2) b1, b2 (O1) b3 (O2)			
Reactor length H, cm				
Reactor width T, cm				
Solution level h, cm				
Volumetric flow, Q, $\text{dm}^3 \text{ min}^{-1}$				
a b3 distance from free water level = 1.5 or 6 cm				
<i>Lamp specifications</i>				
	Nominal power, W	Lamp length with uniform light emission L, cm	Lamp radius R_l , mm	Irradiances at lamp wall ^a $I_w, \text{W m}^{-2}$
(a) UVA blacklight blue lamp (T5, Phillips)	8	21.3	7.75	$I_{w,UVA} = 89.4$
Full-spectra tropical sunlight lamps				
(b1) Narva Biovital®, T5, UVB	24	55	7.75	$I_{w,UVA} = 34.6$ $I_{w,UVB} = 29.7$
(b2) Exoterra, T8, Repti Glo 2.0	20	55	13.0	$I_{w,UVA} = 45.1$ $I_{w,UVB} = 23.2$
(b3) Arcadia, T5, Natural Sunlight	8	21.3	7.75	$I_{w,UVA} = 6.5$ $I_{w,UVB} = 2.7$

^a Obtained from radiometric readings using correction factor.

shield at the back wall, to absorb the radiation transmitted through the catalyst suspension.

Both reactors were operated in the flow-through recirculation batch mode, with the liquid recirculating through a well-mixed (vigorously stirred) recirculation vessel ($V_{\text{total},R1} = 2 \text{ L}$, $V_{\text{total},R2} = 0.3 \text{ L}$) using a pulse-free peristaltic pump.

In a typical experiment, 2-HBA was dissolved in ultrapure water (Millipore Milli Q, resistivity = 18 M cm^{-1} , total organic carbon < 1 ppb) at an initial concentration ($C_{0,2-\text{HBA}}$) of 0.2 mmol dm^{-3} and the catalyst was added at the required concentration, under darkness. A predetermined volume of the suspension was transferred to the recirculation vessel of the system and air was bubbled continuously at a rate of 30 mL min^{-1} . The suspension was recirculated between the vessel and the photoreactor under darkness for 30 min to reach an equilibrium, which was confirmed by the invariability of the concentration of 2-HBA. After such time, the light was switched on. The reaction systems were operated at ambient temperature ($T = 22 \pm 2^\circ\text{C}$) at the natural pH of 2-HBA/TiO₂ aqueous solution ($\text{pH} = 4.0$) and the pH did not vary during the photocatalytic experiments. Samples collected at suitable time intervals were filtered through $0.20 \mu\text{m}$ PET filters (CHROMAFIL® PET-20/25) to remove the catalyst particles and promptly analyzed by HPLC-DAD (Shimadzu, mounting a $250 \text{ mm} \times 4.6 \text{ mm}$ SUPELCO C18 column) at 303 nm. The analyses were carried out by binary flow

elution with mobile phase solvents A (0.5:99.5 (v/v) methanol: 0.1 M phosphoric acid) and B (100% methanol) at a flow rate of 0.6 and 0.4 mL min^{-1} , respectively.

2.3. Irradiation sources

The light sources (Table 1) used in the photoreactors were a Philips blacklight-blue TL 8W/08 F8 T5/BLB lamp (a) and full-spectrum compact fluorescent bulbs simulating the solar spectra with high colour rendering Ra98/Class 1A and colour temperature of 6500 K (i.e. daylight characteristic) with different portions of UVB irradiation (b1–3). The photon irradiances were monitored with a radiometer (UVX-UVP Products) using midrange UVB UVX-31 (range 280–340 nm) and longwave UVA UVX-36 sensor (range 335–385 nm) with sensors accuracy of $\pm 5\%$.

The cylindrical lamps end sections were covered with Teflon tape to expose the sections of the lamps (0.213 m in R1 and 0.55 m in R2) emitting an approximately constant photon irradiance (5% error). The photon irradiance of the lamps was measured along the lamp length and circumference and the values were averaged across both directions. The total UV irradiance at the wall of the lamp, averaged across the useful emission spectrum, was estimated considering the spectral response of the sensor and the spectral emission of the lamp [3,24]. Therefore, the total UV irradiance for

lamp (a) was corrected by multiplying the radiometric reading by the integral quotient equal to 1.54.

The emission spectrum of the full-spectra lamps in the UVB and UVA regions were equal to the spectral response of the midrange and longwave UV sensors. The photon flux was also measured on the outer wall of R1 and at the surface of R2. The photon irradiance in the visible at the lamp wall was estimated using manufacturer spectral charts. Values of 552 and 297 W m⁻² for lamps (b1) and (b3), respectively, correspond to the average values given for the visible solar irradiation (400–700 nm) at the ocean level in the northern hemisphere in different times of a year [25].

3. Photocatalytic reactor modeling

3.1. Incident photon flux

The SFM modeling approach of photocatalysts suspensions has been reported elsewhere [3,14,24,26]. In this approach, four sub-models including light emission, light absorption and scattering, fluid-dynamics and the reaction kinetics, are combined with the material and energy balances. Since the light sources used in reactors R1 and R2 were long slim tubes with small radius to length ratios, the emission of radiation by the lamps was modelled using either the Linear Source Spherical Emission (LSSE) or the Extensive Source Superficial Diffuse Emission (ESSDE) model.

The LSSE model assumes that the lamp is a line source with each point of the line emitting radiation in every direction and isotropically [27]. It was further assumed that the radiation emitted by the line source was uniform along the axial direction of the lamp. Under these conditions, the incident photon flux at the wall of the reactor, in which radiation meets the fluid, can be written using dimensionless parameters:

$$I_0 = I_{(\eta R), z*} = \frac{S_L}{4\pi\eta R} \left\{ \arctan \left[\frac{\beta}{2} (2\alpha z* - \alpha + 1) \right] - \arctan \left[\frac{\beta}{2} (2\alpha z* - \alpha - 1) \right] \right\} \quad (4)$$

$$e_{r,z}^a = \frac{\tau_{app} I_0}{\omega_{corr}(1 - \gamma)} \frac{\eta}{(1 - \eta)R} \left[\left(\omega_{corr} - 1 + \sqrt{1 - \omega_{corr}^2} \right) \exp(-\tau_{app} r*) + \gamma \left(\omega_{corr} - 1 - \sqrt{1 - \omega_{corr}^2} \right) \exp(-\tau_{app} r*) \right] \quad (6)$$

$$e_{h,T,z}^a = \frac{\tau_{app} I_0(T)}{\omega_{corr}(1 - \gamma)} \left[\left(\omega_{corr} - 1 + \sqrt{1 - \omega_{corr}^2} \right) \exp(-\tau_{app} h*) + \gamma \left(\omega_{corr} - 1 - \sqrt{1 - \omega_{corr}^2} \right) \exp(-\tau_{app} h*) \right] \quad (7)$$

where S_L is the radiation emission of the lamp per unit time and unit length of the lamp ($S_L = 2\pi R_L I_w$), I_w is the radiation intensity measured at the lamp wall, $\alpha = H/L$ and $\beta = L/\eta R$ are the geometrical design parameters of an annular photoreactor where η is the ratio of internal to external diameter of the annulus, and $z^* = z/H$ is the dimensionless axial coordinate of the reactor. The incident photon flux at the inner wall of the reactor was calculated in the UVB (290–340 nm) as $I_{w,UVB}$ and UVA (335–385 nm) as $I_{w,UVB}$, to account for different quantum yields of the oxidation reaction in these regions of the applied full-spectrum lamps, with the sum equals to the radiation intensity measured at the lamp wall I_w .

The ESSDE model has been reported to accurately describe the emission of radiation from fluorescent lamps [28]. This model assumes that equal radiation is emitted by spheres of radius R_L lined one above the other to cover the entire length of the lamp [29]. The transfer of irradiation in space is considered similarly to

the LSSE model. The incident photon flux at the reactor wall using the ESSDE model is given in Eq. (5).

$$I_0 = I_w \frac{R_L}{2} \frac{1}{R_{in}} \left[\frac{z - a}{\sqrt{R_{in}^2 + (z - a)^2}} - \frac{z - a - L}{\sqrt{R_{in}^2 + (z - a - L)^2}} \right] \quad (5)$$

where R_{in} is the inner radius of the annular reactor, z is an axial coordinate, a is the difference between lamp length and reactor height ($2a = H - L$). In the calculations, dimensionless units were used:

$$L^* = L/H$$

$$a^* = a/H$$

The incident radiation reaching the exposed surface of a flat reactor is commonly normalized according to the measured total useful irradiation arriving to reactor surface [13]. In this particular case, lamp radius is approximately four times smaller than reactor width and the incident photon flux was the highest at the centre ($x = 0$, Fig. 1a), while it gradually reduced in intensity towards the side borders of R2, i.e. widthwise ($x = \pm T/2$). The incident photon flux at any (x, z) point on the surface of R2 with the ESSDE model was calculated by observing from different angles each of the emitting spheres stacked over the length of the lamp (Fig. 1a). The reactor x coordinate (width) of the reactor was converted into cylindrical coordinates applying simple geometry. The R_{in} was set as the range from $R_{in,0}$ to $R_{in,N}$, which corresponded to $x = 0$ and $x = \pm T/2$, respectively, and the incident photon flux at the free surface of flat reactor was calculated accordingly by summing up the radiation arriving from each sphere.

3.2. Radiation field and rate of photon absorption

A schematic representation of R1 and R2 geometries in terms of cylindrical and Cartesian coordinate systems is shown in Fig. 1b. The radiation field inside the aqueous catalyst suspension was modeled by the SFM, which for an infinitely long annular photocatalytic reactor takes the form (cylindrical coordinates) [3,26]:

$$e^a = \frac{\tau_{app} I_0}{\omega_{corr}(1 - \gamma)} \frac{\eta}{(1 - \eta)R} \left[\left(\omega_{corr} - 1 + \sqrt{1 - \omega_{corr}^2} \right) \exp(-\tau_{app} r*) + \gamma \left(\omega_{corr} - 1 - \sqrt{1 - \omega_{corr}^2} \right) \exp(-\tau_{app} r*) \right] \quad (6)$$

and for an infinite flat reactor takes the form (Cartesian coordinates) [30]:

$$e^a = \frac{\tau_{app} I_0(T)}{\omega_{corr}(1 - \gamma)} \left[\left(\omega_{corr} - 1 + \sqrt{1 - \omega_{corr}^2} \right) \exp(-\tau_{app} h*) + \gamma \left(\omega_{corr} - 1 - \sqrt{1 - \omega_{corr}^2} \right) \exp(-\tau_{app} h*) \right] \quad (7)$$

where e^a is the local volumetric rate of photon absorption (LVRPA) at the coordinates (r, z) (Eq. (6)) or (h, T, H) (Eq. (7)) in the reaction space. For consistency, the axial coordinate in R2 (reactor length) will be marked as z instead of H hereafter. Note that photon absorption in the flat reactor varies along the x, y, z coordinates (h, T, H). In the SFM the radial coordinate r^* from an annular reactor matches the x coordinate in the flat reactor, h^* .

The parameters of the SFM are shown in SI, Table S2. τ_{app} in Eqs. (6)–(7), is the apparent optical thickness, ω_{corr} is the corrected scattering albedo, η is the ratio of the internal to the external radius of the annulus, γ is a SFM dimensionless parameter and r^* and h^* are the dimensionless radial and transversal coordinates, respectively, in the reaction space. The significance of the model parameters have been discussed elsewhere [3] and are presented in Supporting Information. In the SFM the optical properties of the catalyst are represented by spectral-averaged specific scattering σ^* and absorption κ^* coefficients per unit mass of catalyst, respectively. These are calculated by the average of κ_λ^* and σ_λ^* measured experimentally over the useful spectrum of the incident radiation

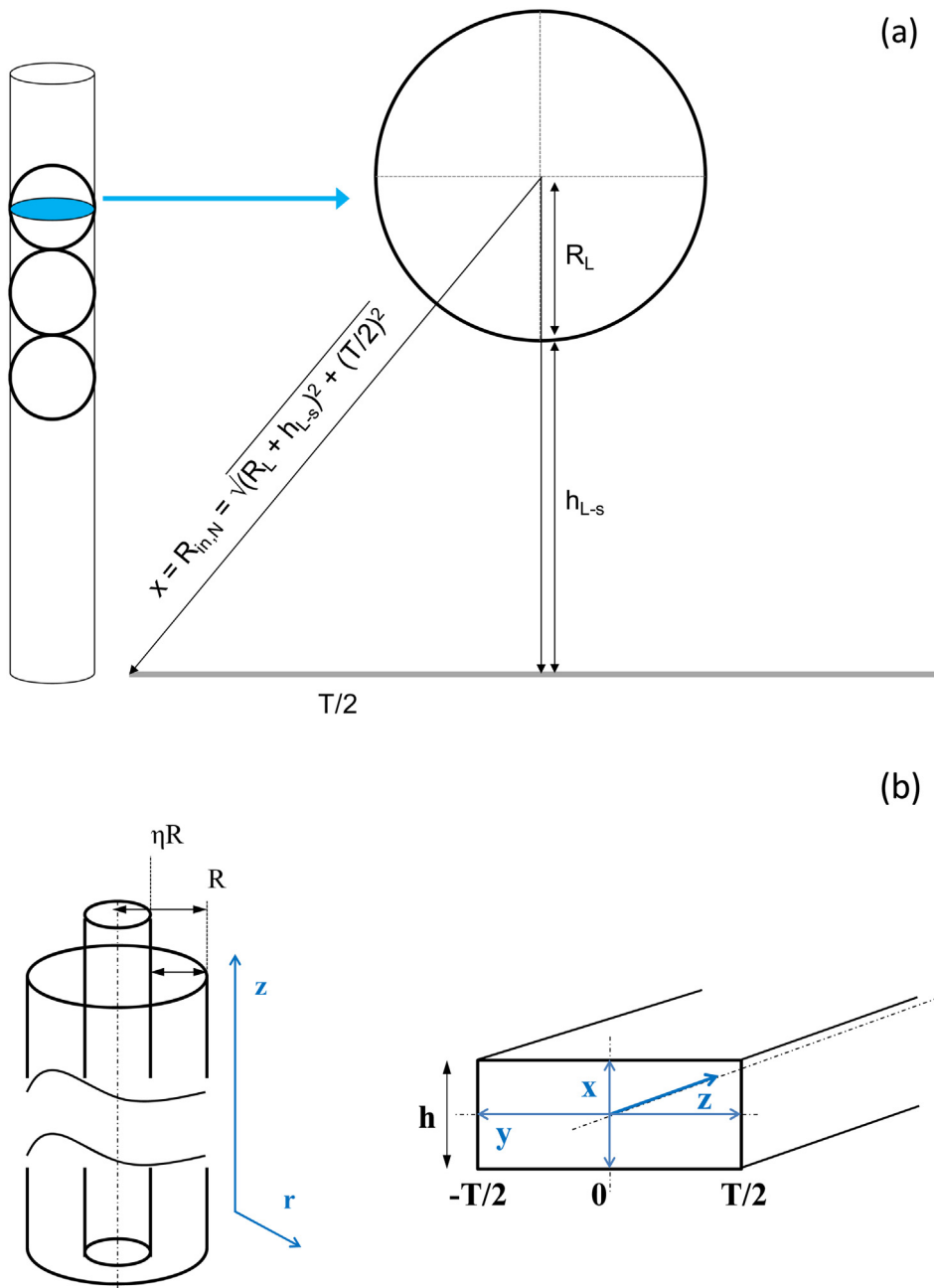


Fig. 1. (a) Schematics of characteristic proportions for calculation of the incident irradiation in a flat reactor; (b) Description of R1 and R2 geometric characteristics.

(i.e., for TiO_2 Degussa P25, $\lambda_{\max} < 384 \text{ nm}$). p_f , p_b and p_s are SFM model parameters which correspond to the probabilities of forward, backward and side scattering, respectively. In this study for simplicity the isotropic scattering model was assumed, with the values $p_f = p_b = p_s = 1/6$.

3.3. Fluid-dynamics

With reference to the reactor geometries described in Fig. 1b their hydrodynamics and irradiation conditions, the concentration of 2-HBA in R1 varied both radially and axially, while in R2, varied in both directions of the rectangular space (h, T) and along the length (H).

Both reactors were operated in the laminar flow regime with Reynolds numbers of 45 for R1 and 46 for R2.

Assuming steady-state, unidirectional laminar flow of Newtonian fluid, the radial velocity profile in R1 was modeled with [24]:

$$v_z = \frac{2Q}{\pi R^2 \left[(1 - \eta^4) - \frac{(1 - \eta^2)^2}{\ln(1/\eta)} \right]} \left[1 - (r_*)^2 + \left(\frac{1 - \eta^2}{\ln(1/\eta)} \right) \ln(r_*) \right] \quad (8)$$

where Q is the volumetric flow rate through the annulus, while for R2, the two-dimensional velocity distribution was obtained by considering the basic equation of the flow (Eq. (9)) where $u(x, y)$, dP/dz and μ are the streamwise velocity, pressure gradient and fluid viscosity in the reactor space/channel, respectively.

$$\frac{\partial^2 u}{\partial x^2} + \frac{\partial^2 u}{\partial y^2} = \frac{1}{\mu} \frac{dP}{dz} = \text{const} \quad (9)$$

The hydrodynamics in R2 was described as laminar flow through the rectangular open channel, with the following assumptions: (i)

steady laminar flow regime; (ii) Newtonian fluid with constant density and viscosity at the working temperature ($\rho = 1000 \text{ kg m}^{-3}$ and $\mu = 0.001 \text{ Pa s}$); (iii) no-slip of fluid at the reactor walls; (iv) zero velocity gradient at free water surface.

The exact analytical solution of Eq. (9) in finite series form is given by the well-known Poiseuille velocity profile for flow through a rectangular channel [31,32], Eq. (10).

$$u(x, y) = \frac{4h^2}{\mu\pi^3} \left(-\frac{dP}{dz} \right) \sum_{n=0}^{\infty} (-1)^n \left\{ 1 - \frac{\cosh[(2n+1)\pi x/h]}{\cosh[(2n+1)\pi T/2h]} \right\} \frac{\cos[(2n+1)\pi y/h]}{(2n+1)^3} \quad (10)$$

In Eq. (10), $-T/2 \leq x \leq T/2$ and $-h \leq y \leq h$. The pressure gradient, which is constant along the z direction, was calculated from Eq. (11), considering the Darcy friction factor (f), Eq. (12) [33] and the average fluid velocity (v_{av} , m s^{-1}), in R2 (Eq. (13)).

$$\frac{dP}{dz} = f \frac{H}{d_H} \frac{\rho v_{av}^2}{2} \quad (11)$$

$$f = \frac{24}{Re} \left[1 - 1.3553 \frac{h}{T} + 1.9467 \left(\frac{h}{T} \right)^2 - 1.7012 \left(\frac{h}{T} \right)^3 + 0.9564 \left(\frac{h}{T} \right)^4 - 0.2537 \left(\frac{h}{T} \right)^5 \right] \quad (12)$$

$$v_{av} = \frac{Q}{V_{R2}} \quad (13)$$

3.4. Reaction kinetics

Previous results of photocatalytic degradation kinetics of salicylic acid indicated that the degradation rates of its photocatalytic oxidation over illuminated photocatalyst followed an apparent Langmuir–Hinshelwood (L–H) kinetics model [34]. The kinetic rate equation (Eq. (14)) used to represent the photodegradation of 2-HBA was derived by considering the following assumptions:

1. The rates of photocatalytic oxidation of 2-HBA can be fitted by a L–H kinetic rate equation
2. The equilibrium constants of the reaction intermediates with the photocatalyst approach the value of the equilibrium constant of 2-HBA.
3. At each point in the reaction space, the rate of the reaction is considered to be proportional to the m^{th} power of the total irradiation absorbed in the reactor (e^a) and to the n^{th} power of the local 2-HBA concentration.

$$r_{2-\text{HBA}} = \frac{k_{2-\text{HBA}} K_{L-H}}{1 + K_{(L-H)} C_{0,2-\text{HBA}}} C_{2-\text{HBA}}^n (e^a)^m \quad (14)$$

For the reactors with full-spectrum lamps irradiation, the contributions from the UVA and UVB regions of the spectrum were handled separately in terms of the incident photon flux I_0 and local volumetric rate of photon absorption (e^a). In the same manner, the photocatalytic degradation of 2-HBA was modeled using both e^a_{UVA} and e^a_{UVB} .

$$r_{2-\text{HBA}} = \frac{k_{2-\text{HBA}} K_{L-H}}{1 + K_{(L-H)} C_{0,2-\text{HBA}}} C_{2-\text{HBA}}^n [(e^a_{\text{UVA}})^{m_1} + (e^a_{\text{UVB}})^{m_2}] \quad (15)$$

For the case in which the photocatalyst showed absorption in visible part of spectrum (Fig. 4), the rate equation was modified to

consider the contribution of e_{vis}^a to the rate and quantum yield:

$$r_{2-\text{HBA}} = \frac{k_{2-\text{HBA}} K_{L-H}}{1 + K_{(L-H)} C_{0,2-\text{HBA}}} C_{2-\text{HBA}}^n \{ [e_{\text{UVA}}^a(r, z)]^{m_1} + [e_{\text{UVB}}^a(r, z)]^{m_2} + [e_{vis}^a(r, z)]^{m_3} \} \quad (16)$$

The photoreactors were operated in flow-through mode by recirculation of the fluid through a well mixed vessel. The coupled differential equations are:

$$V_{\text{Tank}} \frac{d[2-\text{HBA}]_{\text{Tank}}^{\text{out}}}{dt} = Q \left([2-\text{HBA}]_{\text{Tank}}^{\text{in}} - [2-\text{HBA}]_{\text{Tank}}^{\text{out}} \right) \quad (17)$$

for the perfectly mixed reservoir tank (additional stirring was necessary to maintain a desired suspension degree) and

$$v_z(r) \frac{d[2-\text{HBA}]}{dz} = r_{2-\text{HBA}}(z, r, t) \quad (18)$$

$$v_z(h, T) \frac{d[2-\text{HBA}]}{dz} = r_{2-\text{HBA}}(z, h, T, t) \quad (19)$$

for the laminar flow annular and flat-rectangular photoreactor. Note that $r_{2-\text{HBA}}(z, r, t)$ and $r_{2-\text{HBA}}(z, h, T, t)$ stand for the local reaction rate in the annular R1 and flat R2, photoreactor respectively.

The concentration of 2-HBA at the inlet to the reservoir tank is a function of time (a permanent non-stationary state), which means that a time-dependent homogeneous concentration of 2-HBA exits the tank volume and re-enter the reactor, R1 that operates in the laminar flow regime was modeled considering streamline flow with negligible mixing in the lateral direction, since the radial concentration gradient of 2-HBA after each pass was small since the Damkohler number was less than 0.1.

In the annular photoreactor the rate of 2-HBA varies along the reactor length (z direction) and across the radius (r direction) of the reactor, respectively, while in the flat-rectangular photoreactor it varies along the reactor length (z), depth (h) and width (T) since the incident photon flux at the free surface was non-uniform. The average concentration of 2-HBA at the reactor outlet was calculated by the integral of the molar flow rate of the contaminant across the cross-sections of the reactors divided the total flow rate:

$$[2-\text{HBA}]_{\text{R1}}^{\text{out}} = \frac{2\pi \int_r^R r v_z [2-\text{HBA}]_r^{\text{out}} dr}{\eta R Q} \quad (20)$$

$$[2-\text{HBA}]_{\text{R2}}^{\text{out}} = \frac{\int_{-T/2}^{T/2} \int_0^h v_z [2-\text{HBA}]_{h,T}^{\text{out}} dh dt}{Q} \quad (21)$$

where the radial distribution of the 2-HBA concentration at the annular reactor outlet section, $[2-\text{HBA}]_r^{\text{out}}$ and spatial distribution at the flat reactor outlet, $[2-\text{HBA}]_{h,T}^{\text{out}}$, were obtained solving Eqs. (6), (7), (14)–(16), (18) and (19) along the (z, r) domain inside R1, and along the (z, h, T) inside R2, with the boundary condition: $[2-\text{HBA}] = [2-\text{HBA}]_{\text{Tank}}^{\text{in}}$ at $z=0$ at all t .

Since the reactors were operated under total recirculation, it follows:

$$[2-\text{HBA}]_{\text{Reactor}}^{\text{out}} = [2-\text{HBA}]_{\text{Tank}}^{\text{in}} \quad (22)$$

$$[2-\text{HBA}]_{\text{Reactor}}^{\text{in}} = [2-\text{HBA}]_{\text{Tank}}^{\text{out}} \quad (23)$$

The numerical simulation was performed dividing the (z, r) and (z, h, T) domains in sufficiently small intervals in each direction. The local velocity and the local volumetric rate of photon absorption for each point in the reaction space were initially computed solving

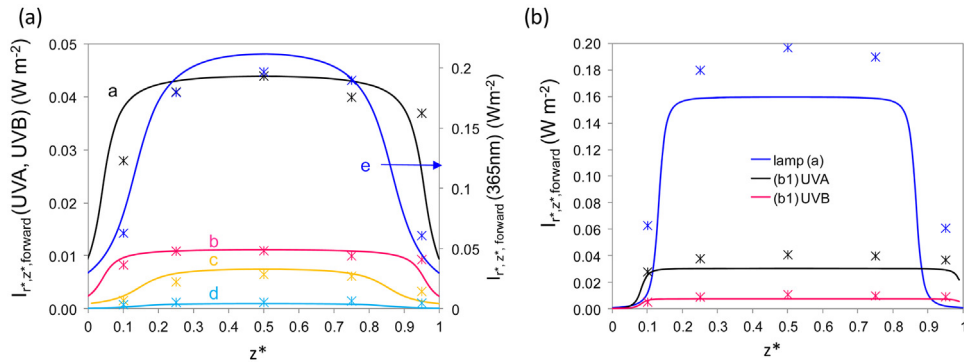


Fig. 2. Forward photon flux emerging from the outer wall of R1 at different positions along the axial direction, $[\text{TiO}_2] = 1.0 \text{ g L}^{-1}$, (a) LSSE and (b) ESSDE model. Legend (a): trace a (lamp b1, $H = 60 \text{ cm}$, outlet O1, UVA); trace b (lamp b1, $H = 60 \text{ cm}$, outlet O1, UVB); trace c (lamp b3, $H = 30 \text{ cm}$, outlet O2, UVA); trace d (lamp b3, $H = 30 \text{ cm}$, outlet O2, UVB); trace e (lamp a, $H = 30 \text{ cm}$, outlet O2).

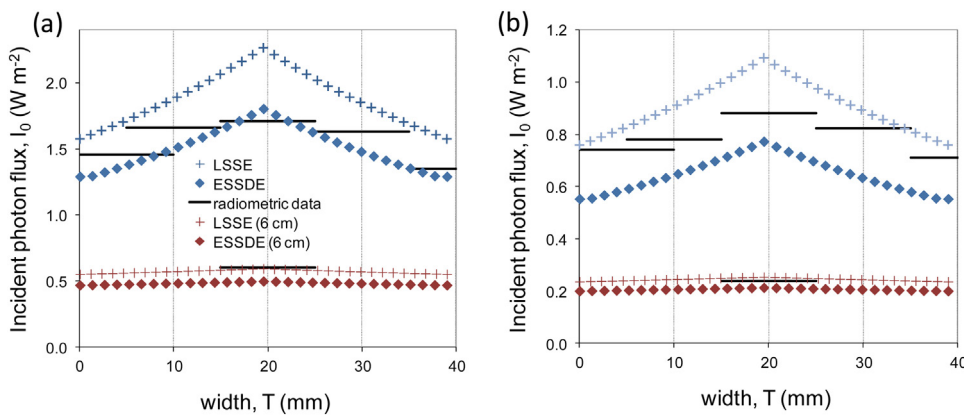


Fig. 3. Incident photon flux on the surface of R2, (a) UVA and (b) UVB irradiation.

Eqs. (4), (6) or (7) and (8) or (10). A small time increment (Δt) equals to the reactor space time ($\tau = V_{\text{Reactor}}/Q$) was then introduced. The mass balance in the tank (Eq. (17)) was then solved for a time period between ($t - \Delta t$) and t considering Eq. (22). Since the reservoir tank was considered to be under ideal mixing conditions then Eq. (23) applied at time t and the material balance in each reactor was solved at time t . The time step counter was increased and the procedure was repeated.

4. Results and discussion

4.1. Comparison of LSSE and ESSDE models

The forward photon flux emerging from the outer wall of R1 at different axial positions was measured using the light sources (**a**) and (**b1**) and compared with the forward photon flux evaluated from the SFM (Eq. (24)) using the radiation emission models (LSSE and ESSDE) [24].

$$I_{(r^*,z^*)\text{,forward}} = \frac{\eta}{r^*} \frac{I_{(\eta R, z^*)}}{1 - \gamma} \left(\frac{2\sqrt{1 - \omega_{\text{corr}}^2}}{1 + \sqrt{1 - \omega_{\text{corr}}^2}} \right) \exp(-\tau_{\text{app}}) \quad (24)$$

The predictions using either LSSE and ESSDE models followed the general trend of the experimental data (Fig. 2), although larger divergences were observed for the reactor fitted with the blacklight-blue lamp (**a**). The LSSE model results in a bell-like shape of the transmitted photon flux, while the ESSDE model gives a more uniform irradiance over the entire lamp span.

The same models were also used for the calculation of the incident photon flux reaching the surface of R2. Bearing that I_0 in R2 varies from the position directly below the lamp towards the reactor sides (Fig. 1a) since the path length of light is increasing, the calculations were limited to the line position directly facing the lamp. The calculation of the incident photon flux using the ESSDE model (Eq. (25)), showed an uniform incident radiation flux along the z direction, since the effective lamps length protruded at least by 5 cm from the reactor R2.

$$I_{R_{in,0} \rightarrow T/2} = I_w R_L^2 \sum_{k=1}^{k=11} \frac{R_{in}(T)}{\left[R_{in}(T)^2 + (z - 2(k-1)R_L)^2 \right]^{3/2}} \quad (25)$$

Note that z is the axial (length) coordinate, and k is the number of spheres. A simple calculation results in 11 spheres in the useful part of the lamp ($k = L_{\text{eff}}/2R_L = 10.97 \approx 11$), where L_{eff} is the effective lamp length matching the reactor length.

The incident photon flux was also calculated using a modified LSSE equation (Eq. (26)) where $\beta' = L_{\text{eff}}/R_{in}(T)$.

$$I_0 = I_{T^*,z^*} = \frac{I_w R_L}{2R_{in}(T)} \left\{ \arctan(\beta' z^*) - \arctan[\beta(z^* - 1)] \right\} \quad (26)$$

The results in Fig. 3 show radiometric readings depicted with black lines, since the sensor surface ($\approx 1 \text{ cm}$) covered $\frac{1}{4}$ of the reactor width (T interval). Nevertheless, it was observed that the radiometric readings fell between the predictions by the LSSE and ESSDE models, for both UVA and UVB irradiation. In consequence,

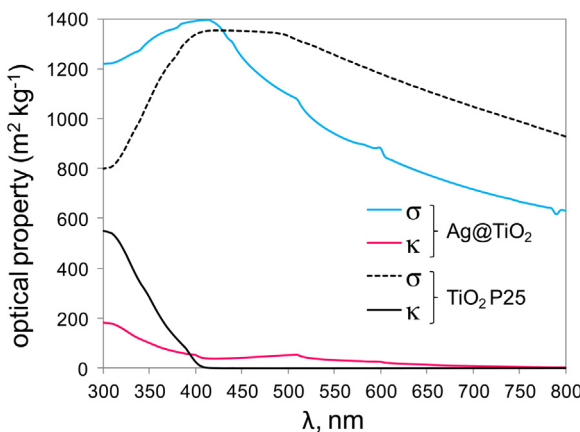


Fig. 4. Optical properties of TiO_2 P25 and $\text{Ag}@\text{TiO}_2$ photocatalysts.

Table 2
Optical properties and kinetic data used in model related to photocatalyst.

photocatalyst	TiO_2 P25	$\text{Ag}@\text{TiO}_2$
σ^* , $\text{m}^2 \text{kg}^{-1}$		
UVA	1175.1	1340.2
UVB	1016.1	1230.7
365 nm	1180.5 (1163) ^a	1344.6
κ^* , $\text{m}^2 \text{kg}^{-1}$		
UVA	189.9	38.4
UVB	508.5	125.4
365 nm	188.5 (187)	78.9
$k_{2-\text{HBA}}$, $\text{kmol m}^{-1.5} \text{s}^{-0.5} \text{W}^{-0.5}$	$(1.50 \pm 0.10) \times 10^{-10}$	
$K_{\text{L-H}}$, $\text{m}^3 \text{kmol}^{-1}$	$(3.57 \pm 0.03) \times 10^4$	
n	1	
$m_1 = m_2 = m_3 = m$	0.5	

^a Values in brackets are retrieved from Ref. [3].

the average values of I_0 were used to model the photocatalytic degradation of 2-HBA in R2.

4.2. Optical properties of catalysts

The optical properties of the photocatalysts TiO_2 P25 and $\text{Ag}@\text{TiO}_2$ determined along the full spectrum of applied irradiation (Fig. 4) were of the same order as those reported in literature [4], however, significant differences were observed among the values reported for the two photocatalysts. The specific scattering coefficients of $\text{Ag}@\text{TiO}_2$ were to 1.1–1.5 times higher than the corresponding values for TiO_2 P25 in the 400–300 nm range, and as expected $\text{Ag}@\text{TiO}_2$ absorbed also in the visible region of the solar spectrum from 400 up to 800 nm. The spectral-averaged specific mass scattering and absorption coefficients in the UVA and UVB (Table 2) later used in the calculation of the rate of photon absorption, were determined from the results in Fig. 4 by averaging the data over the useful spectrum of the incident irradiation (I_λ) [4], with the upper and lower integration limits defined separately in the UVA and UVB part of the spectra, Eqs. (27) and (28).

$$\sigma^* = \frac{\int_{\lambda_{\min}}^{\lambda_{\max}} \sigma^* I_\lambda d\lambda}{\int_{\lambda_{\min}}^{\lambda_{\max}} I_\lambda d\lambda} \quad (27)$$

Table 3
Optical thicknesses (τ) for results in Figs. 6 and 8.

Data set	Figs. 6a and S1 (TiO_2 in R1)		Fig. 6b (TiO_2 in R2)	
	UVA	UVB	UVA	UVB
a	9.555	10.6722	13.65	15.246
b	19.11	21.3444	13.65	15.246
c	9.555	10.6722	13.65	15.246
d	9.555	10.6722	13.69	–
e	9.583	–	–	–

Data set	Fig. 8a ($\text{Ag}@\text{TiO}_2$ in R1)			Fig. 8b ($\text{Ag}@\text{TiO}_2$ in R2)		
	UVA	UVB	in visible	UVA	UVB	in visible
a	9.6502	9.4927	0 ^a	13.786	13.561	5.507
b	9.6502	9.4927	3.8549	13.786	13.561	5.507
c	–	–	–	14.235	–	–

^a The e_{vis}^a contributing term was excluded from model.

$$\kappa^* = \frac{\int_{\lambda_{\min}}^{\lambda_{\max}} \kappa_\lambda^* I_\lambda d\lambda}{\int_{\lambda_{\min}}^{\lambda_{\max}} I_\lambda d\lambda} \quad (28)$$

The values of σ^* and κ^* of TiO_2 P25 at 365 nm determined using the blacklight-blue lamp irradiation spectra were similar to the values reported in literature [3] (Table 2) reinforcing our confidence in these results. Moreover, the apparent similarity between the scattering albedo in the current study (Table 2) and in our previous studies [3,24] suggested a similarity of the prevailing conditions of the catalyst suspension in the diluted aqueous solution of contaminant, i.e. the TiO_2 agglomeration degree was insignificantly affected by changes in solution pH, TiO_2 concentration and contaminant type.

The estimated average specific scattering and absorption coefficients of $\text{Ag}@\text{TiO}_2$ in the visible region were 546.0 and $4.7 \text{ m}^2 \text{kg}^{-1}$, respectively, with an absorption maximum around 510 nm ($\kappa^* = 52.4 \text{ m}^2 \text{kg}^{-1}$). It is worth to note that the specific absorption coefficients of $\text{Ag}@\text{TiO}_2$ under visible irradiation (400–800 nm) were always higher than those reported for TiO_2 P25, while on average 4 times smaller compared to TiO_2 P25 in the UV region (Fig. 4).

It was observed that the specific scattering and absorption coefficients of $\text{Ag}@\text{TiO}_2$ averaged in the whole spectrum (300–800 nm), σ_{wsa}^* and κ_{wsa}^* were 696 and $18.3 \text{ m}^2 \text{kg}^{-1}$, respectively, which is the same order of magnitude as those reported for TiO_2 P25 under solar irradiation (542 and $28.7 \text{ m}^2 \text{kg}^{-1}$) [30].

4.3. Local volumetric rate of photon absorption

In a reaction system with suspended photocatalytic particles, the volumetric distribution of photon absorption in the reaction space is essential to determine local reaction rates and summing these up, the overall degradation of contaminants. The spatial distribution of the LVRPA in R1 ($e_{\text{r},z}^a$) and R2 ($e_{\text{h},T}^a$) calculated with the SFM using a 1.0 g L^{-1} suspension of TiO_2 P25 is shown in Fig. 5a–f, for three light irradiation conditions: with the blacklight-blue lamp (peak emission at 365 nm), and considering the UVA and the UVB components emitted by the full-spectra lamps. In both reactors, a sharp transversal gradient of the LVRPA was observed from the front surface with minimal photon losses at the reactor back surface, since the optical thicknesses (Table 3) exceeded the optimal values (approximately 3) [13]. In the annular reactor R1, a longitudinal gradient of LVRPA was observed (Fig. 5a–c) since the

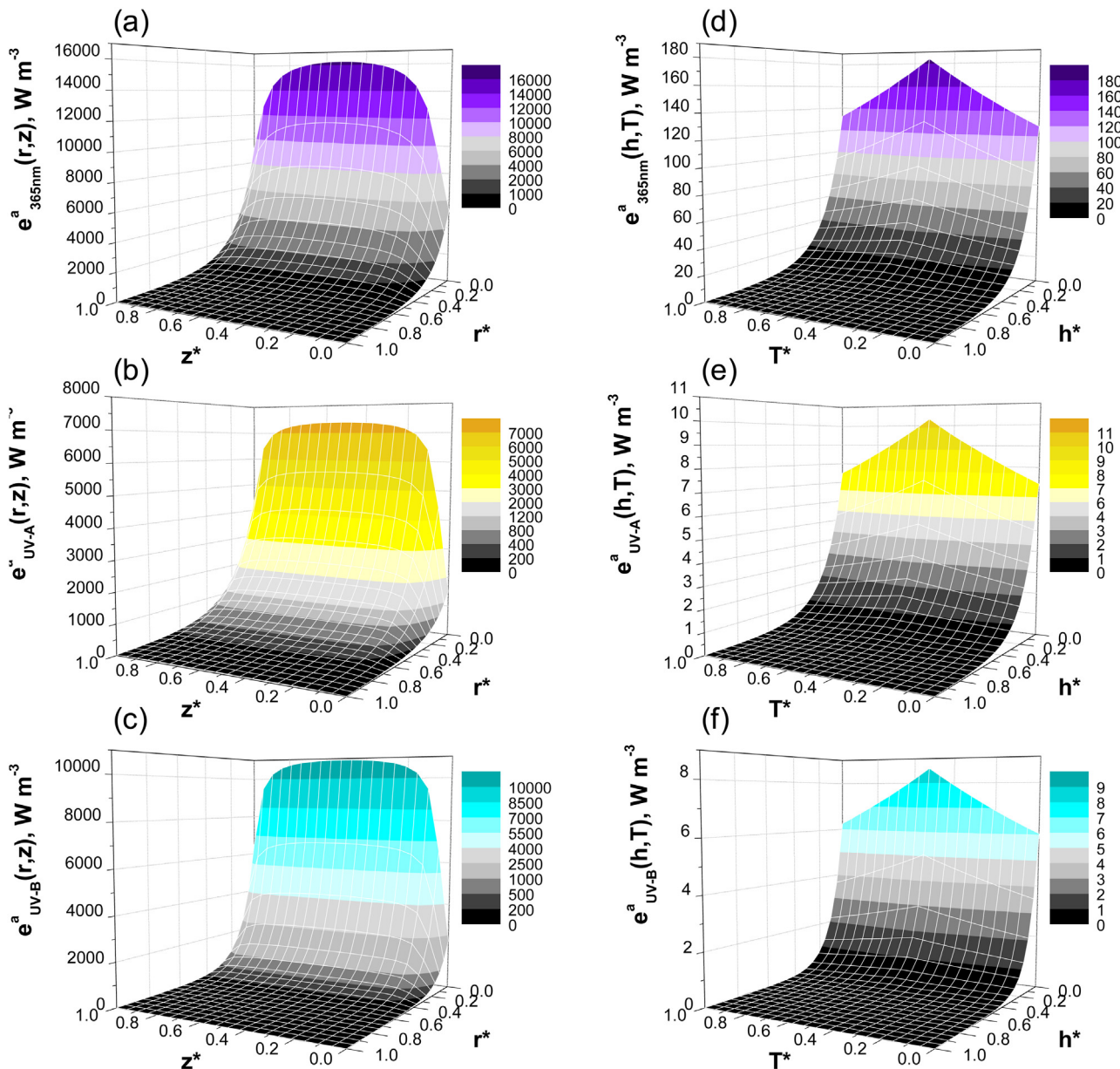


Fig. 5. Spatial distribution of local volumetric rate of photon absorption at 365 nm in R1 with lamp **a**, (a) with the UVA (b) and UVB (c) components of the full spectrum **b1** lamp, and in R2 with lamp **a** (d) located 6 cm away from the surface, and with the UVA (e) and UVB (f) components of the full spectrum **b3** lamp located 6 cm away from the surface. $[\text{TiO}_2] = 1.0 \text{ g L}^{-1}$.

reactor length H slightly exceeded the lamp length L (Table 1). The LVRPA transversal gradient with the UVA component of the full spectrum lamp (Fig. 5b) was less sharp than the corresponding gradient observed with the UVB component (Fig. 5c), since the extinction coefficient ($\beta_\lambda^* = 1365 \text{ m}^2 \text{ kg}^{-1}$) of the TiO_2 suspension averaged over the UVA component of the lamp emission spectrum was smaller than the extinction coefficient ($\beta_\lambda^* = 1525 \text{ m}^2 \text{ kg}^{-1}$) averaged over the UVB component of the lamp spectrum. Fig. 5d–f shows the LVRPA in the flat reactor R2 at the middle axis of the reactor ($z^* = 0.5$). Although the model predicted a further gradient in LVRPA along the axial coordinate (not shown), this effect was negligible since $H \ll L$ (Table 1). The LVRPA profile along the reactor width (x coordinate) followed a trend of incident photon fluxes in R2. Photon absorption rates under the given conditions decreased when approaching reactor boundaries ($x = \pm T/2$). Hence, it is important that the width of reactors with the flat surface is properly designed to avoid regions with poor illumination. Opti-

mal operation of wider reactors would require multiple irradiation sources.

The LVRPA in the UVA and UVB intervals of the radiation emission spectrum of lamps b1 and b3 were calculated separately and consequently separately introduced in the kinetic rate law (Eq. (15)) to reflect the differences in the quantum yields for the contaminant oxidation reaction.

4.4. Modeling the photocatalytic oxidation of 2-HBA

The photocatalytic oxidation of 2-HBA over irradiated aqueous suspensions of TiO_2 P25 and $\text{Ag}@\text{TiO}_2$ was studied in the annular reactor R1 and flat reactor R2, under different irradiation conditions. The model results shown correspond to the SFM with isotropic scattering phase function, since it was shown that either isotropic scattering or the diffusely reflecting phase functions could model the experimental results of the photocatalytic oxidation of

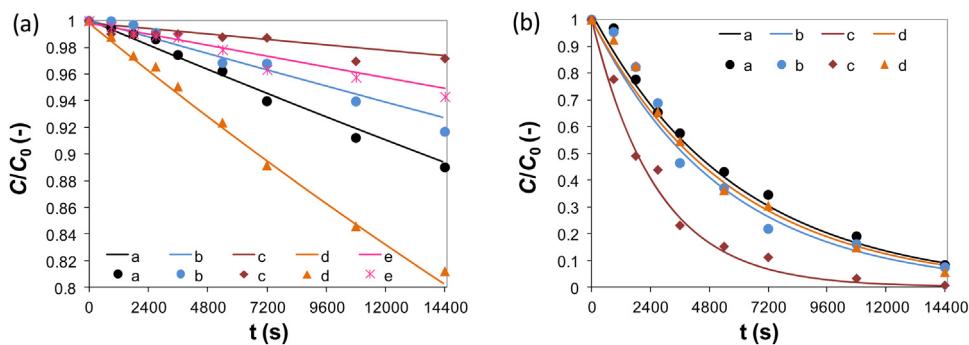


Fig. 6. Kinetics of 2-HBA photocatalytic oxidation in R1 (a) and R2 (b) using TiO_2 P25. Legend (a): trace a ($[\text{TiO}_2] = 1.0 \text{ g L}^{-1}$, outlet O1, lamp **b1**); trace b ($[\text{TiO}_2] = 2.0 \text{ g L}^{-1}$, outlet O1, lamp **b1**); trace c ($[\text{TiO}_2] = 1.0 \text{ g L}^{-1}$, outlet O2, lamp **b3**); trace d ($[\text{TiO}_2] = 1.0 \text{ g L}^{-1}$, outlet O1, lamp **b2**); trace e ($[\text{TiO}_2] = 1.0 \text{ g L}^{-1}$, outlet O2, lamp **a**). Legend (b): trace a (lamp **b3** located 6.0 cm above the free surface, flow rate $0.033 \text{ dm}^3 \text{ min}^{-1}$); trace b (lamp **b3** located 1.5 cm above the free surface, flow rate $0.067 \text{ dm}^3 \text{ min}^{-1}$); trace c (lamp **b3** located 1.5 cm above the free surface, flow rate $0.067 \text{ dm}^3 \text{ min}^{-1}$); trace d (lamp **a** located 1.5 cm above the free surface, flow rate $0.033 \text{ dm}^3 \text{ min}^{-1}$). Symbols are experimental data. Lines are model predictions using the LSSE model.

oxalic acid [3]. The inherent differences in the representation of the scattering phenomena by these two different phase functions appear to have a minor effect, and any significant effect on the local volumetric rate of photon absorption is overruled because of the half-order dependence of the rate from e^a in the region with high photon flux. The model included the estimation of local reaction rates from Eqs. (7), (15), (17), (19), (21)–(23).

In the absence of strong radial mixing, as in case of studied flow-through photoreactors R1 and R2, which were operated in the laminar flow regime, the local reaction rates of 2-HBA photocatalytic degradation were estimated and integrated over the entire reactor volume. The analysis was also carried out through modeling of the radiation field by SFM and considering the incident photon flux distribution to the reactor entrance surface, especially in case of R2, whereby the incident photon flux varied along the reactor width. The decrease in the $I_0(x)$ values with $x \rightarrow \pm T/2$ in combination with estimated local velocities resulted in significant variations in $e^a(h, T)$ along the x coordinate (Fig. 5d–f). The latter should not be ignored, since the model predictions for local contaminant degradation rates strongly depends on accurately calculated $e^a(h, T, z)$.

Fig. 6 shows the results obtained in R1 and R2 for a set of experimental conditions and the model fitting, when the catalyst concentration (TiO_2 P25) was 1.0 and 2.0 g L^{-1} . The radiation emission was modeled using either the LSSE model (Eq. (4), Fig. 6) or the ESSDE model (Eq. (5), SI, Fig. S1). These two radiation emission models produced similar results. Although R1 volume was 4.70 times larger than R2, the apparent 2-HBA degradation rates observed in R1 (Fig. 6a) were much less than in R2 (Fig. 6b). On first sight, this effect can initially be attributed to the total volume of the fluid in R1, which was 6.67 times higher than in R2. However, the incident photon flux in R1 was 10 fold higher than in R2 and this effect should compensate the difference in fluid volumes. Such large difference cannot be explained in simple terms and the reasons would have to be found elsewhere. It may be argued that the first-order dependence of the contaminant degradation rate observed at lower photon fluxes (in R2) may have contributed somewhat to explain the results, since at higher photon fluxes (in R1) such dependence becomes half-order. However, in reality the reactor hydrodynamics (laminar flow velocity profiles) and the matching of these profiles with the LVRPA transversal profiles, played the most significant role in the reaction rates observed in the two reactors, especially

since the photoreactors were operated at optical thicknesses much higher than optimum (Table 3). In R1 (Fig. 6a) the rate at higher catalyst loading (2.0 g L^{-1} , trace b) had an adverse effect on the 2-HBA degradation rates in comparison to the results obtained with half the catalyst loading (1.0 g L^{-1} , trace a). However, such effect was not observed in R2 (Fig. 6b). The reason for this apparent contradiction has to be attributed to the matching of LVRPA radiation field and fluid velocity profiles [13]. If we assume the TiO_2 particles uniformly distributed in the aqueous solution and that the local velocity of the catalyst particles matches the local velocity of the fluid, under the conditions of laminar flow, as is the case, the TiO_2 particles are primarily moving in the longitudinal direction in both reactors. In consequence, the level of irradiation that each fluid element receives in the reactor determines the overall conversion of 2-HBA. The velocity and LVRPA profiles in R1 (Fig. 7a) and R2 (Fig. 7b) are shown in Fig. 7. It is clearly shown that in R1 with 2.0 g/L catalyst concentration a large fraction of the catalyst suspension travelling at the fastest speed (near the middle of the annulus) does not absorb radiation since this is extinguished nearer to the reactor front surface. However, such fraction is greatly reduced when the catalyst concentration was reduced to 1.0 g/L and for this reason the observed degradation of 2-HBA increased (Fig. 6a).

In marked contrast, in R2 the fluid travelling at the fastest speed, having the shortest residence time, absorbed the greatest amount of radiation, and therefore the observed 2-HBA degradation rates in R2 were significantly higher than in R1. In R2 the degradation of 2-HBA with 1.0 and 2.0 g/L catalyst concentration were similar (Fig. 6b, trace a and b), within the range of the experimental errors, since there is a match between the LVRPA and velocity profiles [13] and the impact of having different LVRPA profiles becomes less significant. The results obtained with other lamp configurations and outlet streams from R1 and R2 also show the accuracy of the model to fit the experimental results (Fig. 6, traces c–e).

The models presented assumed the coefficients m_1 and m_2 both equal to 0.5, although has been reported that these may vary between 0.5 and 1, tending to 1 at smaller values of the intensity of the incident radiation and viceversa. A sensitivity analysis was therefore performed to evaluate the effect of these coefficients on the model prediction and to justify the assumption of well-irradiated reactor systems. The standard error of the model from the experimental results collected after 4 h of photocatalytic treatment was evaluated with:

$$\text{st. error} = \sqrt{\frac{1}{N-2} \left[\sum \left((C/C_0)_{\text{exp}} - \overline{(C/C_0)_{\text{exp}}} \right)^2 - \frac{\left[\sum \left((C/C_0)_{\text{mod}} - \overline{(C/C_0)_{\text{mod}}} \right) \left((C/C_0)_{\text{exp}} - \overline{(C/C_0)_{\text{exp}}} \right) \right]^2}{\sum \left((C/C_0)_{\text{mod}} - \overline{(C/C_0)_{\text{mod}}} \right)^2} \right]} \quad (29)$$

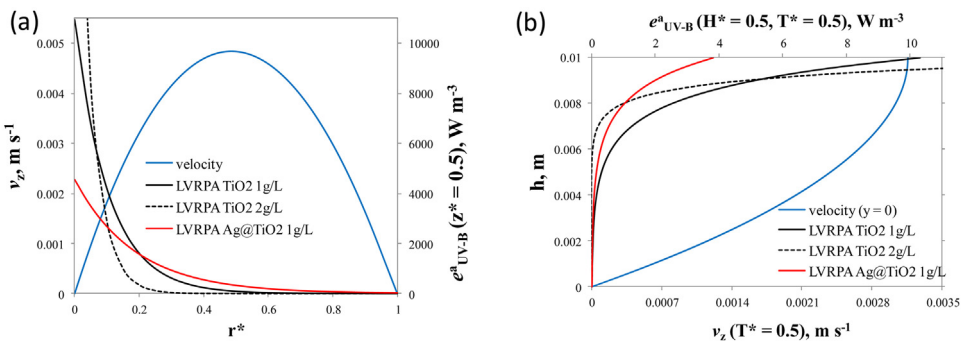


Fig. 7. Transversal profiles of fluid velocity and local volumetric rate of photon absorption (only e^a_{UVB} is shown) at different catalysts loadings in R1 (a) and R2 (b).

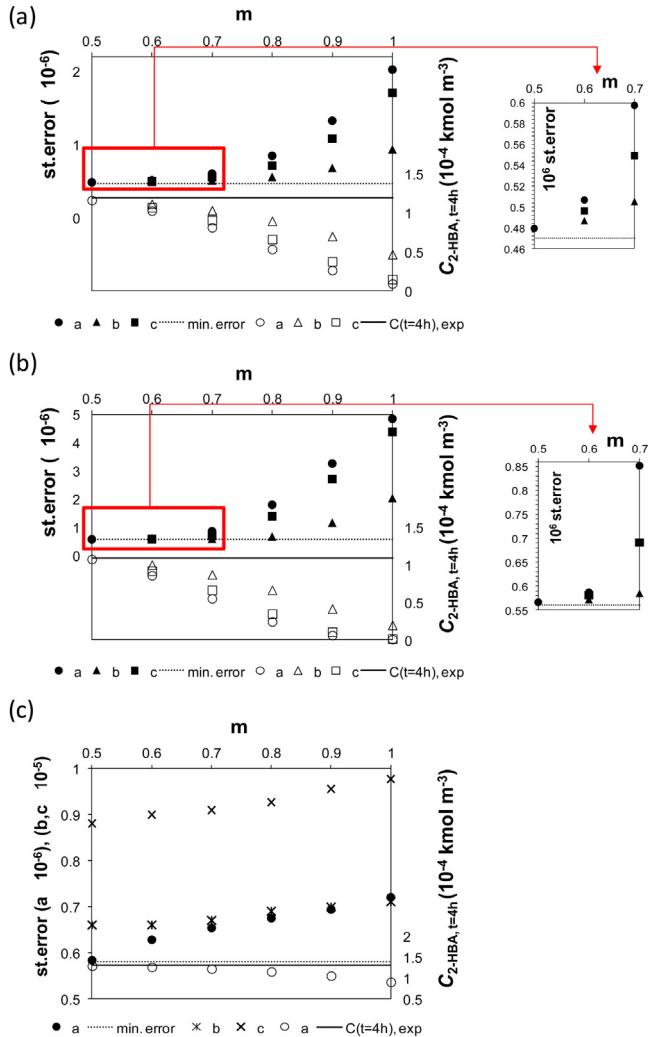


Fig. 8. Standard errors and deviations in the concentration of 2-HBA after 4 h treatment with variable exponents m_1 and m_2 . (a) Lamp b1 in R1 and (b) lamp b2 in R1: trace a (both m_1 and m_2 varied); trace b ($m_1 = 0.5$ and m_2 varied); trace c ($m_2 = 0.5$ and m_1 varied). (c) Lamp b3: trace a (R1); trace b (R2, lamp located 6.0 cm above the free surface); c (R2, lamp located 1.5 cm above the free surface). Filled symbols represent the standard error. Hollow symbols represent the concentration of 2-HBA, $C_{2\text{-HBA},4\text{h}}$, calculated from the model with the above conditions.

where N is the number of data points, $(C/C_0)_{\text{mod}}$ and $(C/C_0)_{\text{exp}}$ are the normalized 2-HBA concentration predicted by the model and from the experiments, respectively. The $(C/C_0)_{\text{mod}}$ and $(C/C_0)_{\text{exp}}$ are corresponding mean (average) values [35].

The results of this analysis (Fig. 8) show that in R1, an exponential error was produced as m_1 and/or m_2 approached unity. When the reactor was irradiated with lamp (b1), which emitted more UVB irradiation than natural sunlight, varying m_1 and m_2 between 0.5 and 1, equally contributed to the increase in the standard errors (Fig. 8a, trace a) but the error was significantly higher when lamp (b2) was used (Fig. 8b). Furthermore, the error appears more apparent when the coefficient m_1 was varied (keeping the other coefficient equal to 0.5) rather than m_2 (Fig. 8a and b, traces b and c).

Since lamp (b2) emitted a significantly higher proportion of UVA and less UVB radiation in comparison to lamp (b1), the larger sensitivity of the model to the parameter m_1 , may suggest that a square root dependence of the LVRPA in the 2-HBA rate law may be more appropriate since such dependence is characteristics of high radiation intensities.

The lamp (b3) emitted less quanta of irradiation than lamps b1 and b2 (Table 1). As anticipated, lower UVB and UVA emissions in R1 resulted in lower standard errors calculated with both m_1 , $m_2 \rightarrow 1$ (Fig. 8c, trace a). The situation is similar in R2 and the error increased in linear trend, irrespective of the distance of the lamp to the free surface in reactor R2 (Fig. 8c, traces b and c). Lamp b3 was characterized with 2–3 times lower UVB emission compared to UVA, meaning that the parameter m_2 could be varied from 0.5 to 1, with negligible influence on the calculated 2-HBA degradation rates. Ideal hydrodynamic conditions in R2 and direct exposure of the photocatalyst to the incident irradiation resulted in more than 50% of 2-HBA oxidized after 1 h of treatment (Fig. 6b). Note that the incident UVB and UVA irradiation in R2 (at 1.5 cm distance from lamp) correspond to the average levels of UVB and UVA irradiation on a partially sunny/cloudy day in early spring in the northern hemisphere (40–50°).

The effect of the water matrix was investigated performing photocatalytic experiments with 2-HBA spiked into pure, lake and tap water. The results revealed similar rates of 2-HBA oxidation on the different water matrices (SI, Fig. S2.) Moreover, its primary intermediates: 2,5-dihydroxy benzoic acid and 2,3-dihydroxybenzoic acid followed the predicted kinetics (SI, Fig. S2 and Table S3).

The model (Eqs. (6), (16)–(18), (20), (22), (23)) was also applied to fit the experimental results of 2-HBA photocatalytic oxidation in R1 and R2 (Fig. 9) using the Ag@TiO₂ photocatalyst (1.0 g L⁻¹) and in R2 varying the lamp distance (1.5 and 6.0 cm). The LVRPA was calculated separately over the UVB, UVA and visible range of the lamp emission spectrum considering the optical parameters, σ^* and κ^* calculated over each range and these were inserted in the rate equation (Eq. (16)), which remarkably simplified the overall modeling procedure.

The modeling of the oxidation of 2-HBA oxidation over irradiated Ag@TiO₂ suspensions in R1 required the inclusion of the full emission spectrum of the lamp (trace b). Neglecting the contribu-

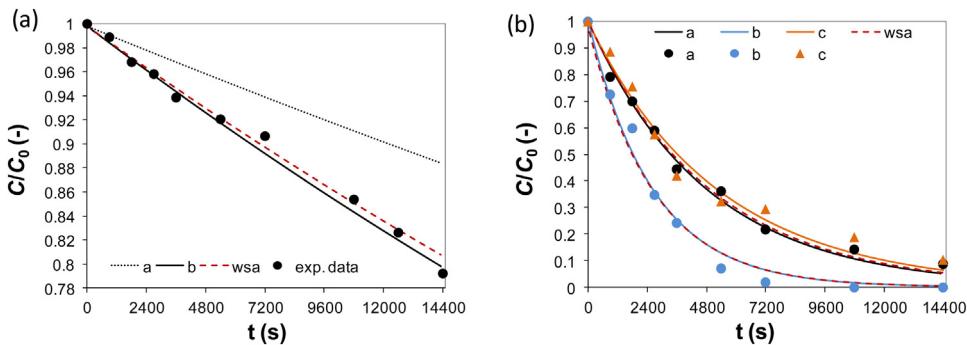


Fig. 9. Kinetics of 2-HBA photocatalytic oxidation in R1 (a) and R2 (b) using $1.0 \text{ g L}^{-1} \text{ Ag@TiO}_2$. Legend (a): trace a (outlet O₂, lamp **b3**, model predictions with e^a_{UVB} and e^a_{UVA}); trace b (outlet O₂, lamp **b3**, model predictions with e^a_{UVB} , e^a_{UVA} and e^a_{vis}). Legend (b): trace a (lamp **b3** located 6.0 cm above the free surface, flow rate $0.033 \text{ dm}^3 \text{ min}^{-1}$); trace b (lamp **b3** located 1.5 cm above the free surface, flow rate $0.067 \text{ dm}^3 \text{ min}^{-1}$); trace c (lamp **a** located 1.5 cm above the free surface, flow rate $0.033 \text{ dm}^3 \text{ min}^{-1}$). Symbols are experimental data. Lines are model predictions using the LSSE model. Traces wsa denotes modeling results by Eq. (30).

tion of visible light to the reaction rate (trace a) produced a poor fit of the experimental data. It is further shown that the model also fitted the experimental results in R2 for lamps located at different distances from the free surface and therefore for different incident photon fluxes.

The trace wsa in Fig. 9a and b refers to the model results for the wide-spectra averages and those results were obtained when the σ^*_{wsa} and κ^*_{wsa} were calculated over the whole range (300–800 nm) and were inserted in the simplified rate equation (Eq. (30)). Note that e^a_{wsa} was calculated using estimated light emission for the whole spectrum ($I_{\text{w,wsa}}$) from lamp efficiency and lumens provided by the manufacturer technical data. The $I_{\text{w,wsa}}$ were 619 and 311 W m^{-2} for lamps (b1) and (b3), respectively.

$$r_{2-\text{HBA}} = \frac{k_{2-\text{HBA}} K_{L-H}}{1 + K_{(L-H)} C_{0,2-\text{HBA}}} C_{2-\text{HBA}} (e^a_{\text{wsa}})^{0.5} \quad (30)$$

In R1, there is a small deviation from the results presented by traces b and wsa (Fig. 9a), while in case of R2, the difference is insignificant. For application purpose, having the discrete averages can be more reasonable when dealing with different irradiation conditions, if reactor material absorbs some portion of incident light etc. Moreover, UVA and UVB intensities alone can be determined more accurately than the average total intensity of the whole spectrum, especially since most of the visible light is unimportant for excitation of a wide range of photocatalysts.

The results confirmed that separating the contributions of UVB, UVA and visible radiation and taking discrete averages of the catalyst optical properties allowed accurate modeling of degradation of 2-HBA in different photocatalytic reactors irradiated with wide spectrum radiation sources, at varying levels of UV and visible light irradiation, and operated under different hydrodynamics and using catalysts with different optical properties.

The L-H parameters of the kinetic model ($k_{2-\text{HBA}}$, $\text{kmol m}^{-1.5} \text{ s}^{-1} \text{ W}^{-0.5}$ and K_{L-H} , $\text{m}^3 \text{ kmol}^{-1}$) for the photocatalytic oxidation of 2-HBA on both TiO_2 P25 and Ag@TiO_2 suspensions shown in Table 2 were determined by a nonlinear least-squares optimization procedure that resulted in the best fit of the experimental data. The L-H binding constant (K_{L-H}) for TiO_2 P25 was of the same order as reported in literature (e.g., 1.05×10^4 at pH 7 [36], 2.50×10^4 at pH 6 [37] and 6.10×10^4 at pH 2 [38]). Minor discrepancies might be explained by the differences in the solution pH and also by the effect of irradiation, since adsorption parameters determined in dark are not entirely in accordance with those determined under irradiation [3,35]. It is important to note that the L-H kinetic model is valid for both photocatalysts, TiO_2 P25 and Ag@TiO_2 , since both catalysts have the same crystalline composition, specific surface area ($\sim 55.8 \text{ m}^2 \text{ g}^{-1}$) and granulometric properties. The small loading of Ag nanoparticles on TiO_2

surface was not expected to influence the binding of 2-HBA on the TiO_2 surface. The effect of the two catalysts was only taken into account considering the rate of photon absorption since the two materials displayed different optical properties.

The validation of photocatalytic degradation models in different reactors operated under significantly different experimental conditions is infrequently reported in literature. In this study, the SFM, coupled with both LSSE and ESSDE radiation models was applied in two different photoreactor geometries, annular reactor and a rectangular open channel, operated under laminar flow but presenting different hydrodynamics transversal profiles.

The kinetic parameters reported in Table 2 can be considered to be independent from reactor geometry, reactor size, properties of photocatalyst and irradiation conditions, such as intensity and wavelength emission.

5. Conclusions

This study has dealt with the application of a comprehensive model for the photocatalytic degradation of 2-HBA, including radiation emission, propagation through the reactor and absorption. The local volumetric rate of photon absorption, at each position in different photoreactor geometries was evaluated using the six-flux radiation absorption-scattering model (SFM) coupled with either the linear source spherical emission (LSSE) model or the extensive source superficial diffuse emission (ESSDE) model. It was shown that both LSSE and ESSDE models could be successfully applied for the modeling of annular and flat reactors, considering the emission from tubular fluorescent light sources. The Langmuir-Hinshelwood kinetic model for the degradation of a 2-HBA model contaminant, using irradiated aqueous suspensions of either TiO_2 or Ag@TiO_2 photocatalyst, was combined with the SFM to determine local reaction rates, which were further integrated with the reactors hydrodynamics and material balances to model the degradation of 2-HBA in both annular and flat photoreactors. Intrinsic photocatalytic reaction kinetic constants, independent of reactor type, catalyst concentration, irradiance levels, radiation wavelength and hydrodynamics were determined by fitting the experimental data to the model results. It was shown that the model parameters were independent of the type of catalyst used, although the catalyst exhibited different optical properties. This kind of evaluation is important since each catalyst when dispersed in an aqueous suspension might absorb and scatter light photons differently. This study has confirmed the wider applicability and robustness of previously reported SFM, which can be applied with ease to predict the degradation of water contaminants in different photoreactors, under different incident radiation and wavelength and using different photocatalysts.

Acknowledgments

This work was financially supported by the University of Zagreb research funding.

Appendix A. Supplementary data

Supplementary data associated with this article can be found, in the online version, at <http://dx.doi.org/10.1016/j.apcatb.2017.04.014>.

References

- [1] S. Parsons, Advanced Oxidation Processes for Water and Wastewater Treatment, IWA Publishing, London, 2004.
- [2] K. Nakata, A. Fujishima, *TiO₂ photocatalysis: design and applications*, J. Photochem. Photobiol. C 13 (2012) 169–189.
- [3] I. Grčić, G. Li Puma, Photocatalytic degradation of water contaminants in multiple photoreactors and evaluation of reaction kinetic constants independent of photon absorption, irradiance reactor geometry, and hydrodynamics, Environ. Sci. Technol. 47 (2013) 13702–13711.
- [4] J. Colina-Maíquez, F. Machuca-Martínez, G. Li Puma, Photocatalytic mineralization of commercial herbicides in a pilotscale solar CPC reactor: photoreactor modeling and reaction kinetics constants independent of radiation field, Environ. Sci. Technol. 43 (2009) 8953–8960.
- [5] J. Marugán, R. van Grieken, A.E. Cassano, O.M. Alfano, Intrinsic kinetic modeling with explicit radiation absorption effects of the photocatalytic oxidation of cyanide with TiO₂ and silica-supported TiO₂ suspensions, Appl. Catal. B 85 (2008) 48–60.
- [6] M. Salaises, B. Serrano, H.I. De Lasa, Experimental evaluation of photon absorption in an aqueous TiO₂ slurry reactor, Chem. Eng. J. 90 (2002) 219–229.
- [7] R.J. Braham, A.T. Harris, A complete multi-scale simulation of light absorption within a fluidized bed photoreactor using integrated particle, fluid and photon behaviour models, Phys. Chem. Chem. Phys. 15 (2013) 12373–12385.
- [8] G.E. Imoberdorf, F. Taghipour, M. Keshmiri, M. Mohseni, Predictive radiation field modeling for fluidized bed photocatalytic reactors, Chem. Eng. Sci. 63 (2008) 4228–4238.
- [9] J. Colina-Maíquez, F. Machuca-Martínez, G.L. Puma, Radiation absorption and optimization of solar photocatalytic reactors for environmental applications, Environ. Sci. Technol. 44 (2010) 5112–5120.
- [10] M.A. Mueses, F. Machuca-Martínez, G. Li Puma, Effective quantum yield and reaction rate model for evaluation of photocatalytic degradation of water contaminants in heterogeneous pilot-scale solar photoreactors, Chem. Eng. J. 215–216 (215) (2013) 937–947.
- [11] D. Wang, Y. Li, G. Li, C. Wang, W. Zhang, Q. Wang, Modeling of quantitative effects of water components on the photocatalytic degradation of 17 α -ethynodiol in a modified flat plate serpentine reactor, J. Hazard. Mater. 254–255 (2013) 64–71.
- [12] L. Zhang, W.A. Anderson, Z.J. Zhang, Development and modeling of a rotating disc photocatalytic reactor for wastewater treatment, Chem. Eng. J. 121 (2006) 125–134.
- [13] G. Li Puma, Modeling of thin-film slurry photocatalytic reactors affected by radiation scattering, Environ. Sci. Technol. 37 (2003) 5783–5791.
- [14] G. Li Puma, A. Brucato, Dimensionless analysis of slurry photocatalytic reactors using two-flux and six-flux radiation absorption scattering models, Catal. Today 122 (2007) 78–90.
- [15] R.R. Bhosale, S.R. Pujari, G.G. Muley, S.H. Patil, K.R. Patil, M.F. Shaikh, A.B. Gambhire, Solar photocatalytic degradation of methylene blue using doped TiO₂ nanoparticles, Sol. Energy 103 (2014) 473–479.
- [16] S. Chang, W. Liu, The roles of surface-doped metal ions (V Mn, Fe, Cu, Ce, and W) in the interfacial behavior of TiO₂ photocatalysts, Appl. Catal. B Environ. 156–157 (2014) 466–475.
- [17] E.S. Azam, Visible light photocatalytic degradation of thiophene using Ag-TiO₂/multi-walled carbon nanotubes nanocomposite, Ceram. Int. 40 (2014) 6705–6711.
- [18] R.M. Mohamed, E.S. Baeissa, Preparation and characterisation of Pd-hydroxyapatite nanoparticles for the photocatalytic degradation of cyanide under visible light, Appl. Catal. A Gen. 464–465 (2013) 218–224.
- [19] Q.R. Deng, X.H. Xia, M.L. Guo, Y. Gao, G. Shao, Mn-doped TiO₂ nanopowders with remarkable visible light photocatalytic activity, Mater. Lett. 65 (2011) 2051–2054.
- [20] C. McManamon, P. Delaney, M.A. Morris, Photocatalytic properties of metal and non-metal doped novel sub 10 nm titanium dioxide nanoparticles on methyl orange, J. Colloid Interface Sci. 411 (2013) 169–172.
- [21] Y.K. Twu, Y.W. Chen, C.M. Shih, Preparation of silver nanoparticles using chitosan suspensions, Powder Technol. 185 (2008) 251–257.
- [22] R. Lopez, R. Gomez, Band-gap energy estimation from diffuse reflectance measurements on sol-gel and commercial TiO₂: a comparative study, J Sol Gel Sci. Technol. 61 (2012) 1–7.
- [23] M.I. Cabrera, O.M. Alfano, A.E. Cassano, Absorption and scattering coefficients of titanium dioxide particle suspensions in water, J. Phys. Chem. 100 (1996) 20043–20050.
- [24] G. Li Puma, J.N. Khor, A. Brucato, Modeling of an annular photocatalytic reactor for water purification: oxidation of pesticides, Environ. Sci. Technol. 38 (2004) 3737–3745.
- [25] BOON: Bodega Ocean Observing Node, Bodega Marine Laboratory, Solar and Photosynthetically Active Radiation Data charts, <http://www.bml.ucdavis.edu/boon/light.html>, Accessed 11 July 2016.
- [26] B. Toepfer, A. Gora, G. Li Puma, Photocatalytic oxidation of multicomponent solutions of herbicides: reaction kinetics analysis with explicit photon absorption effects, Appl. Catal. B 68 (2006) 171–180.
- [27] S.M. Jacob, J.S. Dranoff, Radial scale-up of perfectly mixed photochemical reactors, Chem. Eng. Prog. Symp. Ser. 62 (1966) 47–55.
- [28] J. Schneider, D. Bahnemann, J. Ye, G. Li Puma, D.D. Dionysiou, Photocatalysis: Fundamentals and Perspectives, The Royal Society of Chemistry, 2016, 2017.
- [29] R. Tsekov, P.G. Smirniotis, Radiation field in continuous annular photocatalytic reactors: role of the lamp finite size, Chem. Eng. Sci. 52 (1997) 1667–1671.
- [30] H.L. Otalvaro-Marín, M.A. Mueses, F. Machuca-Martínez, Boundary layer of photon absorption applied to heterogeneous photocatalytic solar flat plate reactor design, Int. J. Photoenergy (2016) 8, Article ID 930439.
- [31] G.-B. Lee, C.-C. Chang, S.-B. Huang, R.-J. Yang, The hydrodynamic focusing effect inside rectangular microchannels, J. Micromech. Microeng. 16 (2006) 1024–1032.
- [32] F.M. White, Viscous Fluid Flow, McGraw-Hill, New York, 1991.
- [33] R.K. Shah, A.L. London, Laminar Flow Forced Convection in Ducts, Academic Press, Inc., 1978, pp. 196–222.
- [34] A.N. Rao, B. Sivasankar, V. Sadasivam, Kinetic study on the photocatalytic degradation of salicylic acid using ZnO catalyst, J. Hazard. Mater. 166 (2009) 1357–1361.
- [35] I. Grčić, S. Papić, I. Brnardić, Photocatalytic activity of TiO₂ thin films: kinetic and efficiency study, Int. J. Chem. React. Eng. (2017), <http://dx.doi.org/10.1515/ijcre-2016-0153>.
- [36] J. Cunningham, G. Al-Sayed, Factors influencing efficiencies of TiO₂-sensitised photodegradation: part 1. substituted benzoic acids: discrepancies with dark-adsorption parameters, J. Chem. Soc. Faraday Trans. 86 (1990) 3935–3941.
- [37] S.M. Ould-Mame, O. Zahraa, M. Bouchy, Photocatalytic degradation of salicylic acid on fixed TiO₂ – kinetic studies, Int. J. Photoenergy 2 (2000) 59–66.
- [38] A. Mills, C.E. Holland, R.H. Davies, D. Worsley, Photomineralization of salicylic acid: a kinetic study, J. Photochem. Photobiol. A: Chem. 83 (1994) 257–263.